

PAD: Phase-Amplitude Decoupling Fusion for Multi-Modal Land Cover Classification

Huiling Zheng¹, Xian Zhong¹, Senior Member, IEEE, Bin Liu², Member, IEEE, Yi Xiao¹, Graduate Student Member, IEEE, Bihan Wen³, Senior Member, IEEE, and Xiaofeng Li⁴, Fellow, IEEE

Abstract—The fusion of Synthetic Aperture Radar (SAR) and RGB imagery for land cover classification remains challenging due to modality heterogeneity and the underutilization of spectral complementarity. Existing methods often fail to decouple shared structural features from modality-specific radiometric attributes, leading to feature conflicts and information loss. To address this issue, we propose Phase-Amplitude Decoupling (PAD), a frequency-aware framework that separates phase (modality-shared) and amplitude (modality-specific) components in the Fourier domain. Specifically, PAD consists of two key components: 1) *Phase Spectrum Correction (PSC)*, which aligns cross-modal phase features through convolution-guided scaling to enhance geometric consistency, and 2) *Amplitude Spectrum Fusion (ASF)*, which dynamically integrates high-frequency details and low-frequency structures using frequency-adaptive multilayer perceptrons. This approach leverages SAR’s sensitivity to morphological features and RGB’s spectral richness. Extensive experiments on WHU-OPT-SAR and DDHR-SK datasets demonstrate state-of-the-art performance. Our work establishes a new paradigm for physics-aware multi-modal fusion in remote sensing. The code will be available at <https://github.com/RanFeng2/PAD>.

Index Terms—Land Cover Classification, RGB-SAR Multi-modality, Multi-modal Segmentation, Synthetic Aperture Radar, Remote Sensing

I. INTRODUCTION

LAND cover classification (LCC) is a fundamental task in Earth observation that involves categorizing various

Manuscript received April 21, 2025. This work was supported in part by the National Natural Science Foundation of China (Grants No. 62271361 and 42006159) and the Hubei Provincial Key Research and Development Program (Grant No. 2024BAB039). Numerical calculations were partly carried out on the Big Earth Data Cloud Service Platform. (Corresponding authors: Xian Zhong and Bin Liu.)

Huiling Zheng is with the Sanya Science and Education Innovation Park, Wuhan University of Technology, Sanya 572025, China; the School of Computer Science and Artificial Intelligence, Wuhan University of Technology, Wuhan 430070, China; and the Key Laboratory of Ocean Circulation and Waves, Institute of Oceanology, Chinese Academy of Sciences, Qingdao 266071, China (e-mail: zhenghl@whut.edu.cn).

Xian Zhong is with the Hubei Key Laboratory of Transportation Internet of Things, School of Computer Science and Artificial Intelligence, Wuhan University of Technology, Wuhan 430070, China, and the State Key Laboratory of Maritime Technology and Safety, Wuhan University of Technology, Wuhan 430063, China (e-mail: zhongx@whut.edu.cn).

Bin Liu is with the College of Oceanography and Ecological Science, Shanghai Ocean University, Shanghai 201306, China (e-mail: bliu@shou.edu.cn).

Yi Xiao is with the School of Geodesy and Geomatics, Wuhan University, Wuhan 430072, China (e-mail: xiao_yi@whu.edu.cn).

Bihan Wen is with the Rapid-rich Object Search Lab, School of Electrical and Electronic Engineering, Nanyang Technological University, Singapore 639798 (e-mail: bihan.wen@ntu.edu.sg).

Xiaofeng Li is with the Key Laboratory of Ocean Circulation and Waves, Institute of Oceanology, Chinese Academy of Sciences, Qingdao 266071, China (e-mail: xiaofeng.li@ieee.org).

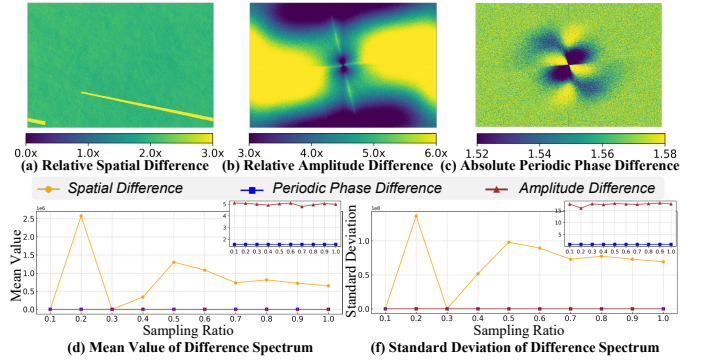


Fig. 1. SAR-RGB Spatial-Frequency Complementarity Analysis. Frequency-domain representations capture modality complementarity more effectively than spatial features. (a) Spatial discrepancies exhibit anisotropic distributions; (b) relative amplitude differences are pronounced in high-frequency regions; (c) phase discrepancies are minimal and clustered in low-frequency bands; (d)–(e) variations in sampling rates significantly affect the spatial discrepancy distribution. Analysis conducted on WHU-OPT-SAR (see Section III-A).

surface materials, such as farmlands, forests, water bodies, and urban areas, using remote sensing imagery. This capability is essential for environmental monitoring, resource management, and urban development [1]. In recent years, fusing Synthetic Aperture Radar (SAR) and RGB imagery has emerged as a promising approach to improve LCC performance. SAR provides robust structural information that is less susceptible to atmospheric and illumination variations, while RGB imagery offers rich spectral details, compensating for SAR-specific artifacts such as speckle noise [2], [3].

Despite their complementary relation, a key challenge remains: the inherent imaging heterogeneity between microwave backscattering (SAR) and optical reflectance (RGB), which leads to significant spectral misalignment and hinders the effective fusion of cross-modal features. Compared to conventional multi-modal fusion in natural images, integrating SAR and RGB data presents more pronounced radiometric and geometric disparities, limiting the performance of existing frameworks [4]–[6].

Deep learning methods, particularly convolutional neural networks (CNNs), have achieved notable success in LCC tasks due to their powerful feature extraction capabilities [7]. To mitigate modality heterogeneity in SAR-RGB fusion, most approaches employ dual-branch architectures to independently extract multi-scale features from each modality [8], followed by fusion via simple operations such as element-wise summation, mean aggregation, or channel-wise concatenation, before processing

with a shared decoder or segmentation head. Although this fusion scheme relies on accurately modeling complementary features, the intrinsic heterogeneity between SAR and RGB often impedes the extraction of truly complementary representations. Recent studies, inspired by contrastive learning [9]–[11], have explored aligning highly correlated, modality-shared features to guide complementary feature learning and alleviate inter-modal conflicts. For example, Li *et al.* [12] considered phase as a modality-shared feature and used it as input in the intermediate network stage. However, they not only disregarded high-frequency amplitude patterns, which are essential for terrain delineation, thus limiting the effectiveness of the fusion, but also failed to systematically prove the complementarity of phase between the two modalities.

Through comprehensive spectral analysis (Fig. 1), we identify three critical frequency-domain priors that have been previously neglected: 1) Spatial-domain alignment (Fig. 1(a)) is significantly hampered by anisotropic discrepancies between modalities, rendering direct pixel- or feature-level matching unreliable; 2) Existing phase-based strategies overlook the inevitable slight differences between different frequency bands (Fig. 1(c)), leading to information loss; and 3) Amplitude mismatches between SAR and RGB modalities present different patterns in the high/low-frequency regions, most pronounced in the high-frequency band (Fig. 1(b)), highlighting the need for frequency-aware difference modeling.

Motivated by these insights, we propose a novel fusion method, Phase-Amplitude Decoupling (PAD). The central idea behind PAD is to disentangle SAR and RGB modalities into phase components, which capture modality-invariant structural information, and amplitude components, which encode modality-specific details. By explicitly aligning the shared phase representations, PAD enhances the extraction of complementary amplitude features, thereby reducing feature conflicts caused by cross-modal heterogeneity. Specifically, PAD comprises two key modules: 1) a Phase Spectrum Correction (PSC) module that ensures robust phase alignment across modalities, and 2) an Amplitude Spectrum Fusion (ASF) module that selectively integrates complementary amplitude cues for improved fusion performance.

Our contributions are summarized fourfold:

- Through the systematic analysis of conventional registration datasets, we establish the frequency distribution law of SAR-RGB common patterns (phase) and unique patterns (amplitude) for the first time, providing an interpretable physical prior for multi-source remote sensing fusion.
- We propose a novel spectral decomposition method that orthogonally separates phase (modality-shared) and amplitude (modality-specific) features, effectively resolving feature conflicts in SAR-RGB fusion while maintaining geometric integrity.
- To address phase inconsistencies, the PSC module employs convolution-guided multiplicative scaling to align and enhance critical structural details, ensuring robust fusion.
- The ASF module leverages frequency-domain multilayer perceptrons to dynamically integrate high-frequency (local details) and low-frequency (global structure) components,

capitalizing on the complementary strengths of SAR and RGB data for improved segmentation.

II. RELATED WORK

A. Multi-modal Fusion for Land Cover Classification

While single-modality approaches [13]–[20] have achieved reasonable performance in homogeneous data scenarios, their inability to leverage cross-modal synergies limits their discriminative power in complex environments. SAR-RGB fusion methods generally follow two paradigms: knowledge transfer via domain adaptation and hierarchical feature integration. In this section, we analyze their technical evolution and inherent limitations.

1) *Cross-Modal Transfer Learning*: Transfer learning [21] seeks to adapt knowledge from one modality to another. However, the significant differences between SAR and RGB data often degrade learned representations, limiting their applicability in multi-modal tasks.

2) *Hierarchical Feature Fusion*: Feature fusion strategies have progressed through three developmental phases: a) *Basic Fusion Operators*: Early methods utilized basic operations such as concatenation or weighted summation [22]. However, these approaches are prone to modality dominance and information redundancy in complex scenes. b) *Attention-Guided Fusion*: Spatial-channel attention mechanisms were introduced to address these issues [23], [24]. For instance, MCANet introduces cross-modal attention (MCAM) to model inter-modality dependencies, MRFS [25] develops progressive cycle attention (PC-Att) for infrared-visible fusion, and CMX [26] introduces bidirectional channel-spatial attention to refine cross-modal features. However, most existing attention paradigms have high computational costs. c) *Complementarity-Aware Fusion*: Recent state-of-the-art approaches explicitly model modality-specific and modality-shared components. ASANet [27] uses semantic focusing modules (SFM) to emphasize complementary features, CDDFuse [10] applies contrastive learning to disentangle private and shared representations, and CEN [28] proposes a method that achieves complementary perceptual fusion through dynamic channel exchange and parameter-sharing-independent batch normalization. Furthermore, recent work [12] pioneers phase-structure alignment by leveraging phase information as a cross-modal invariant feature. Despite these advancements, spatial-domain methods still struggle with geometric misalignment and computational inefficiency.

B. Frequency Representation Learning in Vision Tasks

Frequency analysis offers powerful tools to address challenges in spatial fusion [29]–[31]. Three primary application directions are discussed below:

1) *Phase as a Modality-Invariant Representation*: Decoupling amplitude and phase spectra has proven effective in domain generalization (DG), where models trained on multiple source domains must generalize to unseen target domains. In DG, phase spectra encode structural semantics (*e.g.*, object shapes and edges), while amplitude spectra capture modality-specific styles (*e.g.*, illumination and texture patterns) [32], [33]. Early DG methods [34], [35] attempted to disentangle style and

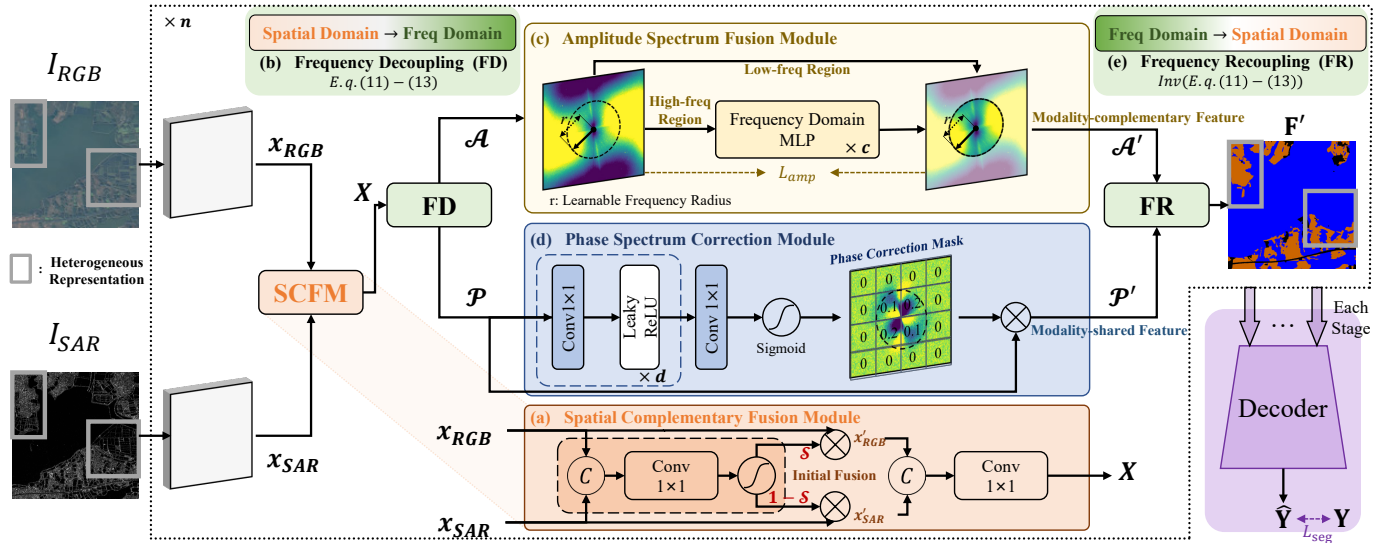


Fig. 2. **Flowchart of the PAD Framework.** The framework comprises the (a) SCF module, (c) ASF module, and (d) PSC module. Registered RGB and SAR images, I_{RGB} and I_{SAR} , are first input, and their features, x_{RGB} and x_{SAR} , are extracted at each backbone stage before being fed into n PAD fusion modules. Meanwhile, (b) FD and (e) FR denote the transformations from the spatial to the frequency domain and vice versa, respectively. Each stage's final output is fed into a shared decoder. Here, \mathcal{A} and \mathcal{P} represent amplitude and phase, and C (outer circle) indicates channel-wise concatenation.

content by normalizing feature statistics (mean/variance), assuming that style corresponds to statistical variations. However, such heuristic separations can distort structural content. Recent approaches employ Fourier transforms as explicit style-content separators. For example, amplitude-phase recombination [36] swaps the amplitude spectrum of a source image with that of a target domain while preserving the source phase, thereby synthesizing cross-domain training samples. This strategy compels networks to focus on phase-centric structural features, improving robustness to style shifts. Building on this, decompose-adjust-compose (DAC) [37] integrates Phase-Amplitude Decoupling with feature normalization to dynamically balance style and content in the frequency domain. These methods highlight a critical advantage of spectral decomposition: phase alignment preserves structural consistency across modalities, while amplitude manipulation enables adaptive style fusion.

2) *Frequency-Driven Global Context Modeling:* Beyond style-content separation, the Fourier transform's global receptive field has been exploited to overcome two key limitations of spatial-domain networks: restricted long-range dependency modeling and the quadratic complexity of self-attention. For instance, fast Fourier convolution (FFC) [38] introduced hybrid spatial-frequency processing with parallel branches, capturing global patterns via spectral operations while preserving local details through convolution. These principles have also been applied to optimize attention mechanisms. FFTformer [39] replaces dot-product attention with spectral element-wise multiplication, reducing complexity from $O(N^2)$ to $O(N \log N)$ while maintaining global interactions. Similarly, GFNet [40] and AFNO [41] employ learnable frequency filters as token mixers, achieving significant speedups compared to efficient self-attention variants. These methods demonstrate that global context aggregation in the frequency domain is not only computationally efficient but also capable of fusing multi-scale information.

3) *Frequency Priors as Inductive Biases:* Recent studies have shown that frequency-domain representations can be explicitly designed as task-specific inductive biases [42]–[44]. For DG, DFF [45] exploits the assumption that low frequencies control cross-domain structural consistency, introducing a frequency-domain dynamic filtering mechanism to amplify domain-invariant components while suppressing high-frequency variations. In dense prediction tasks, FreqFusion [46] applies adaptive frequency filtering: an Adaptive Low-Pass Filter (ALPF) generator smooths high-frequency perturbations to homogenize intra-class features, while an Adaptive High-Pass Filter (AHPF) generator restores critical boundary information lost during downsampling. This strategy encodes spectral priors that low frequencies ensure semantic consistency, while high frequencies enhance boundary discriminability. In the context of RGB-NIR denoising, FCENet [47] utilizes a Frequency Dynamic Selection Module (FDSM) to select useful frequency components across modalities and a Frequency Exhaustive Fusion Module (FEFM) to refine shared and modality-specific spectral features. These approaches demonstrate that decoupling and resetting frequency components effectively encode task-related physical principles, such as structural invariance and boundary sensitivity, injecting strong inductive biases into deep networks.

III. PROPOSED METHOD

This paper introduces a multi-modal fusion framework based on Phase-Amplitude Decoupling (PAD) for land cover classification using SAR and RGB images. PAD effectively integrates complementary information from both modalities while mitigating heterogeneous feature conflicts that often arise with traditional spatial fusion techniques. The overall architecture, depicted in Fig. 2, consists of three main modules: the Amplitude Spectrum Fusion (ASF) module, the Phase Spec-

Algorithm 1: Spectral Difference Analysis.

Input : SAR/RGB image pairs $\{I_{\text{SAR}}^{(i)}, I_{\text{RGB}}^{(i)}\}_{i=1}^N$
Output : RSD, RAD, APPD metrics for each image pair

1: Preprocessing
 //Convert RGB image to grayscale
 1 $I_{\text{RGB}} \leftarrow 0.299 R + 0.587 G + 0.114 B$
 //Retain SAR image as is
 2 $I_{\text{SAR}} \leftarrow I_{\text{SAR}}$

2: Spectral Decomposition
 3 **for each pair** (i) **do**
 //Frequency domain conversion
 4 Compute $\mathcal{A}_{\text{SAR}}^{(i)}$ and $\mathcal{P}_{\text{SAR}}^{(i)}$ via Eqs. (11) to (13)
 5 Compute $\mathcal{A}_{\text{RGB}}^{(i)}$ and $\mathcal{P}_{\text{RGB}}^{(i)}$ similarly
 //Spatial difference computation
 6 Compute $\Delta I^{(i)} \leftarrow \text{RSD}^{(i)}$ via Eq. (1)
 //Amplitude difference computation
 7 Compute $\Delta \mathcal{A}^{(i)} \leftarrow \text{RAD}^{(i)}$ via Eq. (2)
 //Phase difference computation
 8 Compute $\Delta \mathcal{P}^{(i)} \leftarrow \text{APPD}^{(i)}$ via Eq. (3)
 9 **end**

3: Dataset-level Aggregation
 //Mean spatial, amplitude, phase difference computation
 10 $\text{RSD} \leftarrow \text{Mean}(\{\Delta I^{(i)}\}_{i=1}^N)$
 11 $\text{RAD} \leftarrow \text{Mean}(\{\Delta \mathcal{A}^{(i)}\}_{i=1}^N)$
 12 $\text{APPD} \leftarrow \text{Mean}(\{\Delta \mathcal{P}^{(i)}\}_{i=1}^N)$

trum Correction (PSC) module, and the Spatial Complementary Fusion (SCF) module.

A. Frequency-domain Analysis for Modality Decoupling

To validate the physical significance of frequency-domain decoupling in multi-modal data, we conducted a systematic spectral analysis on WHU-OPT-SAR. This analysis includes visualizations of the averaged difference spectra (Fig. 1(a)–(c)) computed using Algorithm 1 to compare the differences between two modalities in different domains. The difference spectra are defined as:

$$\text{RSD} = \frac{1}{N} \sum_{i=1}^N \frac{|I_{\text{SAR}}^{(i)} - I_{\text{RGB}}^{(i)}|}{I_{\text{RGB}}^{(i)} + \epsilon}, \quad (1)$$

$$\text{RAD} = \frac{1}{N} \sum_{i=1}^N \frac{|\mathcal{A}_{\text{SAR}}^{(i)} - \mathcal{A}_{\text{RGB}}^{(i)}|}{\mathcal{A}_{\text{RGB}}^{(i)} + \epsilon}, \quad (2)$$

$$\text{APPD} = \frac{1}{N} \sum_{i=1}^N \left| \arg \exp j(\mathcal{P}_{\text{SAR}}^{(i)} - \mathcal{P}_{\text{RGB}}^{(i)}) \right|, \quad (3)$$

where I_{SAR} , \mathcal{A}_{SAR} , and \mathcal{P}_{SAR} denote the pixel values, amplitude, and phase spectra of SAR images, respectively; I_{RGB} , \mathcal{A}_{RGB} , and \mathcal{P}_{RGB} correspond to those of the RGB images; $\arg(\cdot)$ computes the angle of a complex number; $|\cdot|$ denotes the absolute value; and ϵ is a small constant to prevent division by zero. By leveraging the periodicity of complex exponentials,

TABLE I
STATISTICAL ANALYSIS RESULTS FOR THE AVERAGE PERIODIC PHASE DIFFERENCE SPECTRUM.

Metric	Low Freq	High Freq	Whole Image
Shapiro-Wilk (Stat)	1.0044	1.0050	1.0131
Shapiro-Wilk (p)	1.0	1.0	1.0
Skewness	-0.0521	0.0020	-0.0265
Kurtosis	0.0750	-0.0117	0.0322

APPD maps phase differences into the principal value range $[-\pi, \pi)$, eliminating abnormally large differences caused by phase wrapping (e.g., a true phase difference of 2π is corrected to 0).

Figure 1 reveals three key observations: (1) Spatial differences (RSD) exhibit anisotropic distributions; (2) Amplitude differences (RAD) predominantly emerge in high-frequency regions; (3) Phase differences (APPD) remain minimal with slight low-frequency clustering. The frequency-domain metrics (RAD, APPD) demonstrate superior specificity compared to spatial-domain RSD, confirming that spectral decomposition better captures cross-modal complementarity.

These analyses lead to two fundamental insights that drive our architecture design: *a) Phase Sharing*: The consistently low APPD values indicate strong phase consistency between modalities. This suggests that phase spectra contain shared information that can guide cross-modal learning. Our PSC Module thus performs pixel-level phase alignment while preserving this inherent consistency. *b) Amplitude Complementarity*: The RAD distribution reveals frequency-dependent amplitude divergence, with high-frequency components showing greater discrepancy than low-frequency ones. This localized spectral pattern motivates our ASF Module, which adjusts the frequency radius dynamically to handle frequency-specific amplitude variations.

These phenomena can be physically interpreted based on the inherent characteristics of each imaging modality. Specifically, phase discrepancies manifest differently across frequency bands. Low-frequency disparities primarily stem from geometric distortions in imaging, leading to overall deviation between the two modalities that cannot be registered, whereas high-frequency variations arise from SAR speckle noise affecting fine details. On the other hand, amplitude disparities emerge from varying sensitivities to different ground objects, with low/high frequency contrasts reflecting modality-specific responses to large/small scale structures (e.g., farmlands and forests vs. roads).

We further validate our spectral analysis through sensitivity experiments on sampling rates (Fig. 1(e)–(f)). By analyzing the mean and variance of the difference spectra, we found that both RAD and APPD metrics are largely invariant to sampling rate, confirming that the observed phase-amplitude complementarity originates from intrinsic modality properties, rather than from sampling artifacts.

To assess the statistical consistency of cross-modal phase spectra, we conducted normality tests (Shapiro-Wilk), along with skewness and kurtosis analyses (Table I). Frequency histograms and mean-variance trajectories (Fig. 3) indicate that

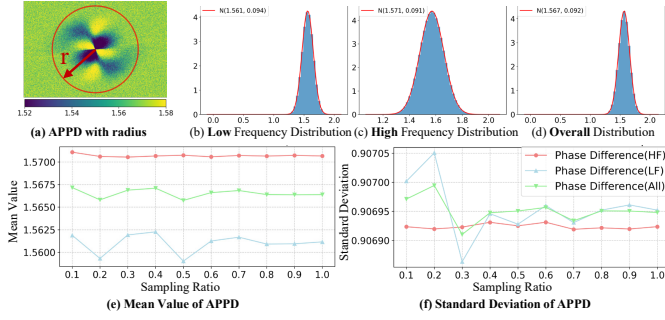


Fig. 3. **Statistical Analysis of APPD.** (a) APPD spectrum; (b)–(d) Frequency histograms with Gaussian fits for low-frequency (LF, **radius = 0.5 × half-diagonal**), high-frequency (HF), and full spectra (ALL); (e)–(f) Mean-variance trajectories across sampling rates. The HF, LF, and ALL spectra show near-Gaussian invariance, while LF/ALL deviates slightly due to the dominant structural noise in the LF range. These results suggest that phase, especially HF, can serve as a robust shared feature.

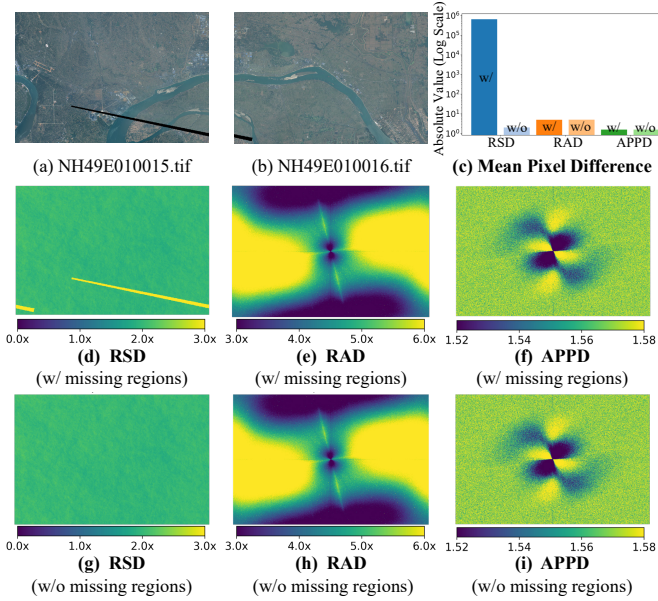


Fig. 4. **Visualization of Spatial and Frequency Spectrum Differences in a Scenario with Missing RGB Regions.** (a)–(b) show RGB images with missing regions; (d)–(f) present the difference spectrum when the missing regions are included; and (g)–(i) display the difference spectrum after excluding the missing regions. (c) indicates that variation in RSD is significantly higher than in RAD and APPD, demonstrating that frequency-domain representations are more robust to missing data.

the frequency difference spectra follow a near-Gaussian distribution, particularly for high-frequency components, whereas low-frequency components exhibit minor systematic deviations, likely due to structural noise.

We also evaluate phase spectrum invariance under challenging conditions through two controlled experiments: (1) *partial RGB data missing* (Fig. 4) and (2) *cloud-obscured observations* (Fig. 5). In the missing RGB scenario, RSD is highly sensitive to data incompleteness (Fig. 4(d) vs. (g)), while phase differences remain consistent (Fig. 4(f) vs. (i)). Similarly, in cloud-affected cases, the APPD variance ($\Delta \approx 10^{-0.037}\%$) is negligible compared to that of RSD ($\Delta \approx 10^{5.81}\%$) and RAD ($\Delta \approx 10^{0.58}\%$) as shown in Fig. 5(d). Collectively, these results demonstrate that phase information (particularly in the high-

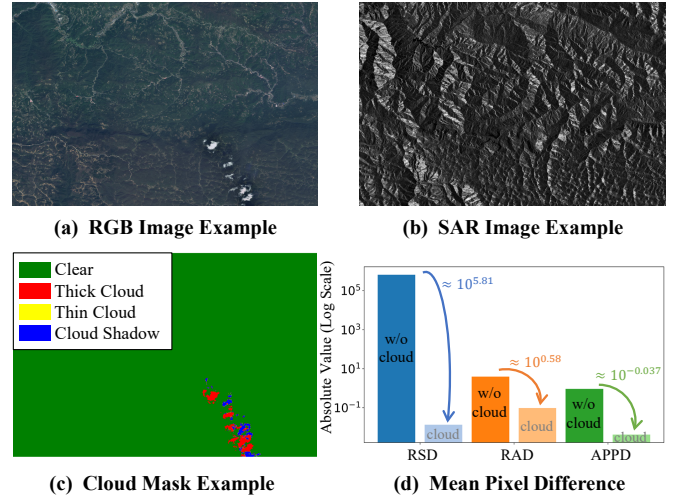


Fig. 5. **Visualization of Spatial and Frequency Spectrum Differences in a Cloud-Obscured Observations Scenario.** (a)–(c) present an example of cloud-obscured observations, with cloud masks generated using RGB, SAR, and NIR images from WHU-OPT-SAR [48]. (d) compares the stability of RSD, RAD, and APPD between cloud-covered and cloud-free regions. Numbers next to the arrow indicates the value of decline.

frequency region) exhibits robust consistency between SAR and RGB modalities, supporting its role as a shared feature to mitigate inter-modal conflicts and leverage complementary information in multi-modal frameworks.

B. Overall Framework

As illustrated in Fig. 2, the proposed PAD framework integrates SAR and RGB modalities via a dual-branch encoder and a shared decoder, with its primary innovation in cross-modal feature fusion through phase-amplitude decoupling. The encoder utilizes *asymmetric convolutional backbones* \mathcal{B}_{SAR} and \mathcal{B}_{RGB} with independent parameters to preserve modality-specific attributes. Specifically, \mathcal{B}_{SAR} extracts microwave scattering features from SAR images, while \mathcal{B}_{RGB} captures optical reflectance patterns from RGB images. Both backbones produce hierarchical feature maps at four stages with resolutions $\{1/4, 1/8, 1/16, 1/32\}$, such that $i \in \{0, 1, 2, 3\}$:

$$x_{\text{RGB}}^i = \mathcal{B}_{\text{RGB}}^i(I_{\text{RGB}}^i), \quad x_{\text{SAR}}^i = \mathcal{B}_{\text{SAR}}^i(I_{\text{SAR}}^i). \quad (4)$$

Initially, the SCF module (Eq. (5)) processes the bimodal features by computing pixel-wise fusion weights through spatial attention gating. This operation preliminarily integrates complementary features in the spatial domain and reduces feature dimensionality, thereby constraining the solution space for subsequent frequency-domain operations.

$$X^i = \text{SCF}(x_{\text{RGB}}^i, x_{\text{SAR}}^i), \quad (5a)$$

$$\mathcal{S} = \text{Sigmoid}(\text{Conv}_{1 \times 1}(\text{Concat}(x_1, x_2))), \quad (5b)$$

$$x'_1 = \mathcal{S} \odot x_1, \quad x'_2 = (1 - \mathcal{S}) \odot x_2, \quad (5c)$$

$$x = \text{Conv}_{1 \times 1}(\text{Concat}(x'_1, x'_2)). \quad (5d)$$

The fused features are then transformed via FD into separate amplitude and phase spectra:

$$\mathcal{A}^i, \mathcal{P}^i = \text{FD}(X^i). \quad (6)$$

The amplitude spectrum \mathcal{A}^i is enhanced by the ASF module, which distinguishes high-frequency details from low-frequency structures using a trainable frequency radius r :

$$\mathcal{A}'^i = \text{ASF}(\mathcal{A}^i; r). \quad (7)$$

Simultaneously, the phase spectrum is corrected via multiplicative scaling in the PSC module:

$$\mathcal{P}'^i = \text{PSC}(\mathcal{P}^i). \quad (8)$$

Finally, FR reconstructs the features, yielding the final fusion output:

$$\mathbf{F}'^i = \text{FR}(\mathcal{A}'^i, \mathcal{P}'^i). \quad (9)$$

The shared decoder, \mathcal{D} , aggregates the multi-stage fused features to generate high-precision land-cover segmentation maps:

$$\hat{\mathbf{Y}} = \mathcal{D}(\mathbf{F}'^0, \mathbf{F}'^1, \mathbf{F}'^2, \mathbf{F}'^3). \quad (10)$$

C. Frequency Decoupling & Frequency Recoupling

To achieve physically disentangled representations in the spectral domain, we propose a bidirectional transformation framework comprising FD and its inverse, FR. First, the input image $X \in \mathbb{R}^{H \times W}$ is transformed from the spatial domain to the frequency domain using a 2D real-valued fast Fourier transform (rFFT) [49], yielding the spectrum $\mathcal{F} \in \mathbb{C}^{H \times W}$:

$$\mathcal{F}(u, v) = \sum_{x=0}^{W-1} \sum_{y=0}^{H-1} X(x, y) \exp\left(-i2\pi\left(\frac{ux}{W} + \frac{vy}{H}\right)\right), \quad (11)$$

where (u, v) represents frequency-domain coordinates. Exploiting the conjugate symmetry of real-valued signals, only the non-redundant region (with $0 \leq u \leq W/2$ and $0 \leq v < H$) is retained. Next, an FFT Shift operation relocates low-frequency components to the center of the spectrum:

$$\mathcal{F}_{\text{shift}}(u, v) = \mathcal{F}\left(u \oplus \frac{W}{2}, v \oplus \frac{H}{2}\right), \quad (12)$$

where \oplus denotes modulo addition. Finally, the amplitude and phase spectra are derived as:

$$\mathcal{A} = |\mathcal{F}|, \quad \mathcal{P} = \angle \mathcal{F}, \quad (13)$$

with $\mathcal{A} \in \mathbb{R}^{H \times W}$ capturing radiometric properties and $\mathcal{P} \in \mathbb{R}^{H \times W}$ preserving structural details. This decoupling enables separate learning of SAR scattering features and RGB structural priors.

D. Phase Spectrum Correction Module

As illustrated in Fig. 1(c), minor misalignments in the low-frequency phase spectra between SAR and RGB images, attributable to inherent geometric distortions (*e.g.*, side-looking SAR vs. RGB orthographic projection), can compromise spatial consistency and boundary precision. Traditional phase alignment methods relying on rigid transformations are inadequate for non-rigid distortions. Thus, we propose a lightweight PSC module that performs adaptive geometric correction using

learnable multiplicative masks. Given an input phase spectrum tensor $P \in \mathbb{R}^{C \times H \times W}$, the module first compresses the channel dimension via a 1×1 convolution (reducing C to C/r , where $r \in \{4, 8\}$) and applies a Leaky ReLU activation [50]. A subsequent 1×1 convolution produces a single-channel Phase Correction Mask (PCM) constrained to $(0, 1)$ by a Sigmoid function. Pixel-wise multiplicative scaling is then applied as follows:

$$P' = P \odot (1 + \text{PCM}), \quad (14)$$

where \odot denotes the Hadamard product. This design limits the maximum scaling factor to 2, ensuring the preservation of phase periodicity while requiring significantly fewer parameters than conventional 3×3 convolutions.

E. Amplitude Spectrum Fusion Module

Our analysis in Fig. 1(b) indicates that the spectral discrepancy between SAR and RGB modalities is primarily concentrated in the medium-to-high frequency components of the amplitude spectra. To exploit this prior while maintaining gradient stability, we design an adaptive spectrum fusion module with three sequential operations. First, we compute a normalized frequency distance metric:

$$\text{Dist}(i) = \frac{\sqrt{(X_i - X_{\text{center}})^2 + (Y_i - Y_{\text{center}})^2}}{\sqrt{X_{\text{max}}^2 + Y_{\text{max}}^2}}, \quad (15)$$

which quantifies component positions relative to the spectrum center $(X_{\text{center}}, Y_{\text{center}})$. A trainable boundary radius r , constrained via a Sigmoid activation to yield $R = \sigma(r)$, dynamically partitions the spectrum into low- and high-frequency regions. To maintain differentiability, a soft partition is employed:

$$\text{Mask}_{\text{high-freq}} = \sigma((\text{Dist} - R) \cdot \tau), \quad (16)$$

with temperature parameter $\tau = 10$. The high-frequency components are then enhanced using a position-wise multilayer perceptron (MLP):

$$A_{\text{high-freq}} = \text{MLP}(A \odot \text{Mask}_{\text{high-freq}}), \quad (17)$$

and concatenated with the original amplitude spectra. A subsequent 1×1 convolution and residual connection yield the fused amplitude:

$$A' = \text{Conv}_{1 \times 1}(\text{Concat}(A, A_{\text{high-freq}})), \quad A \leftarrow A + A'. \quad (18)$$

This module preserves low-frequency structures while adaptively reinforcing high-frequency details that capture complementary semantic information. The learnable radius R self-adjusts to the input characteristics, eliminating the need for manual threshold tuning.

F. Loss Function

Our optimization framework integrates three objectives to jointly promote semantic segmentation accuracy, multi-scale feature learning, and amplitude-phase coherence.

1) *Primary Semantic Supervision*: The primary segmentation loss is defined as the standard cross-entropy loss:

$$\mathcal{L}_{\text{seg}} = - \sum_{i \in \Omega} \sum_{c=1}^C y_{i,c} \log \hat{p}_{i,c}, \quad (19)$$

where Ω denotes the set of foreground pixels (excluding background label 255), $y_{i,c} \in \{0, 1\}$ indicates the ground-truth class, and $\hat{p}_{i,c}$ is the predicted probability.

2) *Auxiliary Semantic Supervision*: An auxiliary segmentation head is added at the second-to-last stage ($t = 2$) using an identical cross-entropy loss:

$$\mathcal{L}_{\text{aux}} = - \sum_{i \in \Omega} \sum_{c=1}^C y_{i,c} \log \hat{p}_{i,c}^{(a)}. \quad (20)$$

3) *Phase-Amplitude Decoupling Constraint*: To resolve the coupling between amplitude and phase spectra, we introduce an Amplitude Consistency Loss that regularizes the fused amplitude \mathcal{A}'_t to remain faithful to its original decoupled state \mathcal{A}_t across feature scales:

$$\mathcal{L}_{\text{amp}} = \frac{1}{|\mathcal{T}|} \sum_{t \in \mathcal{T}} \alpha_t \|\mathcal{A}'_t - \mathcal{A}_t\|_F^2, \quad (21)$$

where $\mathcal{T} = \{0, 1, 2, 3\}$ indexes the feature scales, $\alpha_t = 0.5 + (1.0 - 0.5) \times \frac{t}{3}$ imposes depth-progressive weighting, and $\|\cdot\|_F$ is the Frobenius norm.

4) *Composite Objective*: The overall loss is formulated as:

$$\mathcal{L}_{\text{total}} = \mathcal{L}_{\text{seg}} + \lambda_1 \mathcal{L}_{\text{aux}} + \lambda_2 \mathcal{L}_{\text{amp}}, \quad (22)$$

with $\lambda_1 = 0.4$ balancing auxiliary supervision and $\lambda_2 = 0.1$ controlling the amplitude regularization strength. This composite loss promotes both geometric invariance, by stabilizing phase-sensitive features through \mathcal{L}_{amp} , and semantic invariance via hierarchical amplitude refinement.

IV. EXPERIMENTAL RESULTS

A. Dataset Description

WHU-OPT-SAR [23] is a multi-modal dataset developed for land use classification in Hubei Province, China. The dataset comprises 100 pairs of RGB, near-infrared (NIR), and SAR images covering identical geographic regions, with corresponding land type labels. The RGB images are acquired from GF1 satellite data, while the SAR images are sourced from GF3 satellite data. Both image types have been resampled to a uniform spatial resolution of 5 meters, with dimensions of 5556×3704 pixels. The dataset spans seven primary land use categories: farmland, urban areas, villages, water bodies, forests, roads, and others. In our study, images are cropped into non-overlapping patches of 512×512 pixels, resulting in 7000 total patches; 80% (5600 patches) are used for training and 20% (1400 patches) for testing.

DDHR-SK is a subset of the DDHR multi-modal dataset developed for land cover classification (LCC) in Pohang City, South Korea [24]. RGB images are collected from GF2 satellite data and SAR images from GF3 satellite data. To simulate adverse conditions such as clouds and fog, the RGB images were processed with a fog filter using the GNU Image

Manipulation Program (GIMP). The dataset comprises 6173 paired cloud-affected RGB and SAR images, resampled to a spatial resolution of 1 meter and resized to 256×256 pixels. It covers five land cover types: buildings, farmland, greenery, water, and roads, with a public split of 3087 training images and 3086 validation images.

B. Training Setting

All models were trained and evaluated on a single NVIDIA H800 GPU, while the comparative experiments were carried out on a single NVIDIA A100 GPU. Training was conducted using the MMSegmentation framework [51] with a batch size of 4 and 80k iterations, including validation every 8k iterations. We employed the AdamW [52] optimizer with an initial learning rate of 1×10^{-4} and a Cosine Annealing schedule (with T_max set to the maximum iteration count). A fixed random seed of 42 was used to ensure reproducibility.

Evaluation metrics include mean intersection over union (mIoU), Kappa coefficient, overall accuracy (OA), and F1 score, with performance reported at the iteration yielding the best mIoU. To assess robustness across diverse scenarios and mitigate class imbalance bias, the Kappa coefficient is computed for each sample, and the mean value is reported:

$$\kappa_i = \frac{P_o^{(i)} - P_e^{(i)}}{1 - P_e^{(i)}}, \quad \text{mKappa} = \frac{1}{M} \sum_{i=1}^M \kappa_i, \quad (23)$$

where $P_o^{(i)}$ and $P_e^{(i)}$ denote the observed and expected agreements for the i -th sample, respectively.

C. Experimental Results on Datasets

To assess the effectiveness of the proposed PAD method, we compared its performance with 17 different models, including 9 state-of-the-art multi-modal segmentation approaches and 8 cutting-edge unimodal segmentation methods. All experimental results were obtained through our replication of the original experimental configurations. Experiments were performed on two datasets: WHU-OPT-SAR, the largest multi-modal LCC dataset, and DDHR-SK, which contains RGB images captured under cloudy conditions.

1) *Evaluations on WHU-OPT-SAR*: As summarized in Table II, our PAD framework achieves significant performance improvements on WHU-OPT-SAR. Compared with the best unimodal method (DANet-RGB [13], achieving 53.25% mIoU and 83.19% OA) and the multi-modal baseline MRFS [25] (55.53% mIoU, 84.21% OA), PAD establishes a new state-of-the-art with 56.26% mIoU, 84.56% OA, 53.93% mKappa, and 70.14% mF1. In fine-grained categories, PAD attains 43.24% IoU on Road and 49.70% on Village segmentation, outperforming MRFS by 1.98% and 0.27%, respectively, thereby underlining the precision of our cross-modal fusion strategy.

Visual analyses support these quantitative results. For example, in Fig. 6(a), PAD successfully recovers occluded road segments (highlighted in cyan) in building-dense regions through SAR phase analysis, while RGB-only models ignore these areas. In Fig. 6(b), PAD effectively distinguishes specular

TABLE II
EXPERIMENT RESULTS (%) ON WHU-OPT-SAR.

Method	Venue	IoU per Category							OA	mKappa	mF1	mIoU	
		Farmland	City	Village	Water	Forest	Road	Others					
RGB	DANet [13]	CVPR'19	67.51	55.22	46.71	60.85	83.13	38.89	20.43	83.19	49.74	67.40	53.25
	OCRNet [14]	ECCV'20	67.68	56.48	47.47	61.22	82.98	37.20	17.97	83.23	49.11	66.95	53.00
	CGNet [15]	TIP'20	61.33	45.96	37.98	49.33	80.98	1.92	0.19	79.26	37.42	50.54	39.67
	SegFormer [16]	NeurIPS'21	68.18	56.91	46.82	60.85	83.19	35.24	18.73	83.37	49.46	66.79	52.84
	SETR [17]	CVPR'21	65.25	55.07	42.97	57.80	82.44	31.91	18.36	81.94	46.19	64.73	50.54
	Mask2former [18]	CVPR'22	67.09	56.64	43.97	60.09	81.47	36.24	21.03	82.69	47.69	66.65	52.36
	PIDNet [19]	CVPR'23	66.20	55.20	44.95	58.90	82.20	36.36	16.40	82.25	47.20	65.53	51.46
	TransUNet [20]	MIA'24	67.62	56.28	46.08	60.66	83.25	38.76	19.32	83.18	49.89	67.20	53.14
SAR	DANet [13]	CVPR'19	60.42	54.12	33.05	54.45	80.57	24.89	15.11	79.44	35.28	60.16	46.09
	OCRNet [14]	ECCV'20	59.81	52.48	31.21	54.03	79.57	22.49	13.92	78.94	32.62	58.74	44.79
	CGNet [15]	TIP'20	56.72	46.81	26.32	46.30	77.53	0.27	0.00	76.39	24.64	47.00	36.28
	SegFormer [16]	NeurIPS'21	60.17	54.71	32.30	54.07	79.79	21.02	15.13	79.31	33.60	59.24	45.31
	SETR [17]	CVPR'21	60.35	52.29	31.41	53.56	80.15	18.66	15.18	79.12	34.25	58.33	44.51
	Mask2former [18]	CVPR'22	60.39	52.86	35.69	53.85	78.36	29.16	17.20	79.26	32.76	61.35	46.79
	PIDNet [19]	CVPR'23	58.59	52.35	29.65	53.60	79.35	23.06	13.74	78.42	32.15	58.33	44.34
	TransUNet [20]	MIA'24	61.93	54.85	33.42	56.26	80.63	27.56	14.96	80.14	37.45	61.13	47.09
SAR & RGB	MCANet [23]	JAG'21	64.21	45.49	42.93	56.20	81.81	25.93	8.47	80.80	45.47	59.94	46.44
	CEN [28]	TPAMI'22	66.46	56.28	45.46	58.09	82.34	32.51	17.82	82.32	47.47	65.36	51.28
	TokenFusion [53]	CVPR'22	67.87	57.26	46.96	61.66	83.31	36.34	18.76	83.38	49.87	67.09	53.16
	DDHRNet [24]	JAG'22	59.12	45.67	30.77	47.96	79.59	0.47	0.03	78.00	27.18	48.36	37.66
	CDDFuse [10]	CVPR'23	59.88	35.08	25.22	52.31	78.77	17.64	15.00	77.02	38.69	54.29	40.56
	CMX [26]	TITS'23	69.24	58.20	48.45	64.06	83.83	39.99	<u>21.92</u>	84.18	52.76	69.01	55.10
	MRFS [25]	CVPR'24	69.39	58.13	49.43	64.90	83.87	41.26	21.72	84.21	54.33	69.38	55.53
	FTransUNet [5]	TGRS'24	64.87	53.84	43.71	55.63	81.53	0.00	0.00	81.25	43.53	52.97	42.80
	ASANet [27]	ISPRS'24	69.18	56.95	48.58	64.06	83.79	41.48	21.74	84.15	52.62	69.05	55.11
	PAD (Ours)		69.85	58.10	49.70	65.39	84.05	43.24	23.47	84.56	53.93	70.14	56.26

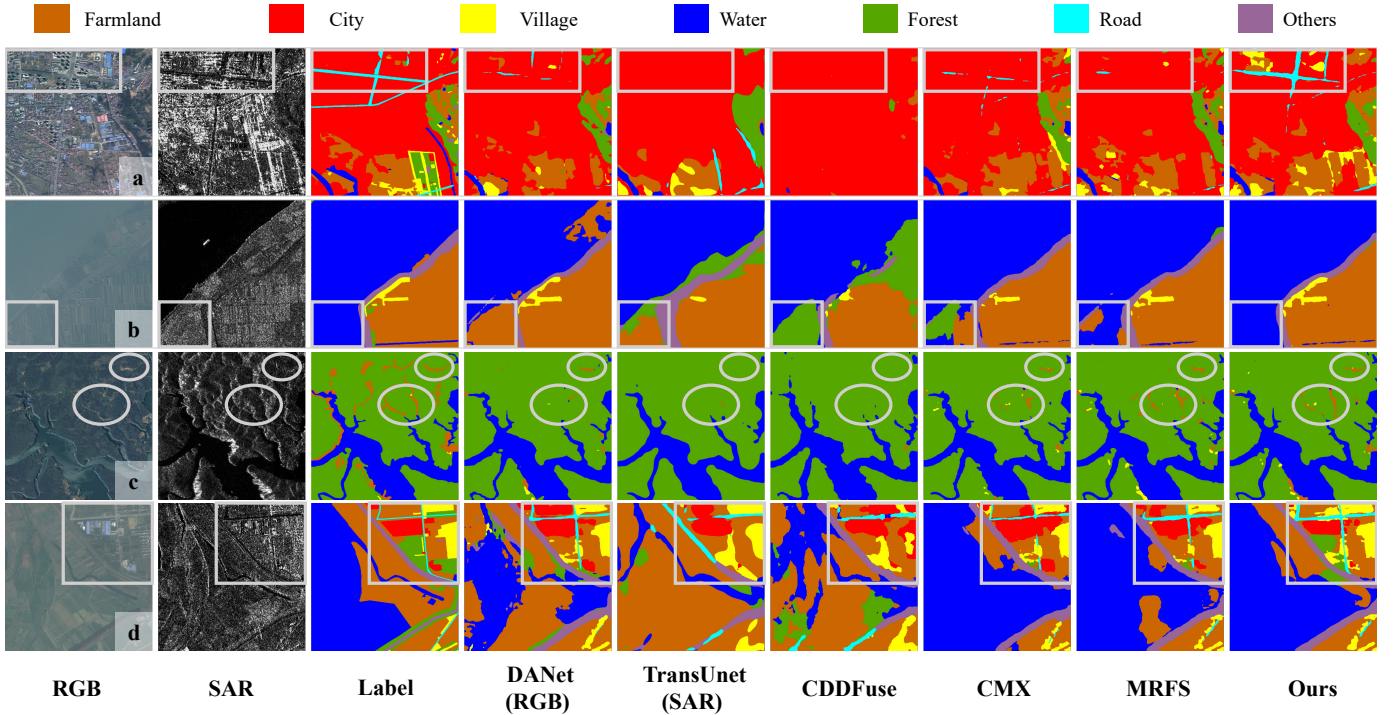


Fig. 6. **Visualization Results on WHU-OPT-SAR.** Four representative cases are shown: (a) building-dense area, (b) specular water bodies, (c) vegetated region, and (d) urban-rural transition zone. For each case, the following images are presented from left to right: RGB image, SAR image, pseudo-color ground truth, and prediction maps from six competing methods. PAD is compared against leading single-modal baselines (DANet-RGB, TransUNet-SAR) as well as multi-modal approaches (CDDFuse, CMX, MRFS). Regions of interest are highlighted with gray boxes (for building/water areas) and circles (for vegetation zones); further details are provided in Section IV-C.

TABLE III
EXPERIMENT RESULTS (%) ON DDHR-SK.

Method	Venue	IoU per Category					OA	mKappa	mF1	mIoU	
		Buildings	Roads	Greenery	Water	Farmland					
RGB	DANet [13]	CVPR'19	94.46	75.11	91.10	99.03	90.59	96.23	73.35	94.57	90.06
	OCRNet [14]	ECCV'20	90.18	60.49	84.42	97.87	82.84	93.17	58.96	90.26	83.16
	CGNet [15]	TIP'20	80.19	27.57	72.77	90.47	69.97	86.16	33.90	78.76	68.19
	SegFormer [16]	NeurIPS'21	92.44	67.11	88.76	98.82	88.18	95.00	66.73	92.71	87.06
	SETR [17]	CVPR'21	94.17	74.10	91.43	99.18	90.88	96.22	73.79	94.49	89.95
	Mask2former [18]	CVPR'22	94.16	80.46	91.08	98.68	86.88	96.07	74.05	94.76	90.25
	PIDNet [19]	CVPR'23	87.77	59.01	80.57	96.89	77.64	91.44	53.43	88.56	80.38
	TransUNet [20]	MIA'24	90.67	62.68	85.64	98.41	83.71	93.64	61.82	90.95	84.22
SAR	DANet [13]	CVPR'19	91.20	58.97	85.93	98.13	82.31	93.57	59.35	90.28	83.31
	OCRNet [14]	ECCV'20	86.38	38.70	78.36	96.18	71.34	89.52	41.07	83.54	74.19
	CGNet [15]	TIP'20	81.16	19.58	69.45	90.27	60.78	84.63	25.42	74.96	64.25
	SegFormer [16]	NeurIPS'21	88.81	46.92	81.99	97.57	76.75	91.51	49.55	86.73	78.41
	SETR [17]	CVPR'21	90.97	59.57	84.71	98.16	80.51	93.27	59.39	89.99	82.79
	Mask2former [18]	CVPR'22	91.34	58.52	86.40	93.29	80.08	93.20	62.69	89.49	81.92
	PIDNet [19]	CVPR'23	84.37	36.77	73.28	94.91	66.91	87.55	38.63	81.49	71.25
	TransUNet [20]	MIA'24	86.56	38.45	77.56	96.53	71.30	89.49	42.21	83.44	74.08
SAR & RGB	MCANet [23]	JAG'21	85.12	47.88	78.69	96.96	73.18	89.59	46.13	85.55	76.37
	CEN [28]	TPAMI'22	91.78	58.73	87.70	98.33	85.73	94.26	60.19	90.93	84.46
	TokenFusion [53]	CVPR'22	93.90	70.67	90.62	98.94	89.21	95.79	69.64	93.70	88.67
	DDHRNet [24]	JAG'22	79.78	13.85	69.85	93.73	62.17	84.73	24.59	73.75	63.88
	CDDFuse [10]	CVPR'23	<u>96.59</u>	83.02	<u>94.59</u>	99.11	93.30	97.61	80.65	96.46	93.32
	CMX [26]	TITS'23	96.43	82.59	<u>94.37</u>	99.38	93.72	97.58	81.08	96.44	93.30
	MRFS [25]	CVPR'24	96.48	<u>83.68</u>	94.48	<u>99.39</u>	<u>93.84</u>	<u>97.65</u>	<u>82.24</u>	<u>96.60</u>	<u>93.57</u>
	FTransUNet [5]	TGRS'24	84.69	35.21	76.51	96.40	71.11	88.56	36.55	82.35	72.78
	ASANet [27]	ISPRS'24	95.04	77.09	92.64	99.24	91.82	96.73	75.77	95.21	91.17
	PAD (Ours)		97.09	86.12	95.38	99.47	94.89	98.04	84.38	97.16	94.59

TABLE IV
ABLATION EXPERIMENTAL RESULTS (%) ON MAIN MODULES ON WHU-OPT-SAR.

ID	Components			IoU per Category							aAcc	mKappa	mF1	mIoU
	MSF	ASF	PSC	Farmland	City	Village	Water	Forest	Road	Others				
I	✗	✗	✗	68.71	57.83	47.34	64.18	83.69	40.90	22.22	83.98	52.11	68.96	54.98
II	✓	✗	✗	69.46	57.16	49.01	65.15	83.87	41.57	21.39	84.32	51.96	69.23	55.37
III	✗	✓	✗	69.45	58.51	48.87	64.22	83.88	<u>43.33</u>	22.73	84.28	53.39	69.77	55.86
IV	✗	✗	✓	69.19	56.16	48.14	65.33	83.61	<u>41.77</u>	21.47	84.15	51.77	69.01	55.10
V	✓	✓	✗	69.91	58.51	49.53	<u>65.52</u>	84.05	42.63	22.58	84.55	54.53	69.93	56.11
VI	✓	✗	✓	<u>69.98</u>	57.32	49.36	65.62	84.12	43.42	23.01	84.57	53.80	69.98	56.12
VII	✗	✓	✓	70.04	58.09	49.19	65.42	<u>84.08</u>	43.11	<u>23.08</u>	84.57	53.79	<u>70.00</u>	<u>56.15</u>
Full Model	✓	✓	✓	69.85	58.09	49.71	65.39	84.05	43.24	23.47	84.56	<u>53.96</u>	70.14	56.26

reflection artifacts from actual water boundaries by leveraging SAR's dielectric properties, overcoming limitations inherent in optical sensors under cloud interference. Additionally, Fig. 6(c) demonstrates PAD's ability to resolve spectral ambiguities in vegetation classification, and Fig. 6(d) shows that PAD maintains cross-category consistency in complex urban-rural transitions.

2) *Evaluations on DDHR-SK*: As shown in Table III, PAD exhibits superior boundary segmentation performance on the relatively simplified scenes of DDHR-SK. Compared with leading unimodal models (e.g., Mask2former-RGB [18], achieving 90.25% mIoU and 94.76% mF1, DANet-SAR [13], yielding 83.31% mIoU and 90.28% mF1) and the multi-modal baseline MRFS [25] (93.57% mIoU, 82.24% mKappa), PAD attains new state-of-the-art performance with 94.59% mIoU, 97.65% OA, 82.24% mKappa, and 96.60% mF1. For boundary-

sensitive categories, PAD achieves 99.47% IoU on Water and 86.12% IoU on Road edges, surpassing MRFS by 2.44% and 0.08%, respectively.

The visual results further reveal PAD's capability in cross-modal boundary refinement. In Fig. 7(a), PAD accurately reconstructs periodically submerged coastal lines via SAR coherence analysis, whereas RGB models tend to confuse tidal sediments with terrestrial areas. In Fig. 7(b), PAD leverages SAR features to delineate water infiltration boundaries in irrigated fields, overcoming the over-segmentation issues common to optical sensors. Moreover, in Fig. 7(c) and Fig. 7(d), PAD achieves continuous road networks under vegetation occlusion and precise material boundaries in vegetation-building complexes, respectively.

3) *Ablation Study*: We performed comprehensive ablation studies on WHU-OPT-SAR to validate the contributions of the

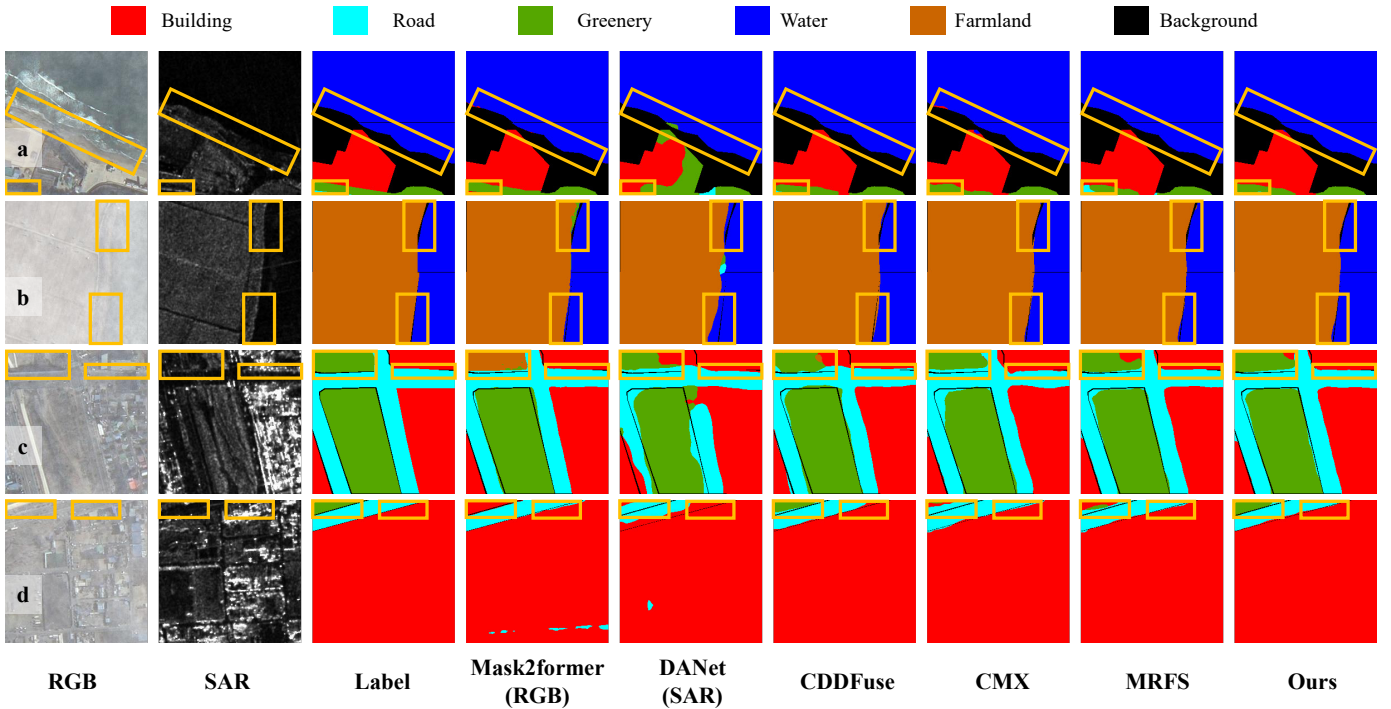


Fig. 7. **Visualization Results on DDHR-SK.** Four boundary-focused cases are shown: (a) coastal demarcation, (b) water–cropland interface, (c) vegetation–building complex, and (d) road network topology. PAD is compared with leading unimodal methods (Mask2former-RGB, DANet-SAR) and state-of-the-art multi-modal approaches (CDDFuse, CMX, MRFS). For each case, the panels display the RGB input, SAR coherence map, pseudo-color ground truth, and prediction maps from six methods. Critical boundary regions are highlighted with orange boxes; further analysis is provided in Section IV-C.

TABLE V
ABLATION EXPERIMENT RESULTS (%) ON LOSS FUNCTION WEIGHTS ON WHU-OPT-SAR.

Configuration	IoU per Category							aAcc	Kappa	mF1	mIoU
	Farmland	City	Village	Water	Forest	Road	Others				
<i>Fixed $\lambda_2 = 0.1$</i>											
$\lambda_1 = 0.01$	69.87	57.71	49.43	65.31	84.12	43.35	23.22	84.54	53.60	70.02	56.14
$\lambda_1 = 0.4$	69.85	58.09	49.71	65.39	84.05	43.24	23.47	84.56	53.96	70.14	56.26
$\lambda_1 = 1.0$	69.56	57.30	49.10	65.39	83.84	41.59	20.97	84.37	52.20	69.21	55.39
<i>Fixed $\lambda_1 = 0.4$</i>											
$\lambda_2 = 0.01$	69.83	56.80	48.67	65.63	84.19	43.17	22.82	84.52	53.54	69.76	55.87
$\lambda_2 = 0.1$	69.85	58.09	49.71	65.39	84.05	43.24	23.47	84.56	53.96	70.14	56.26
$\lambda_2 = 1.0$	69.83	57.74	49.37	64.95	83.95	43.45	22.50	84.46	53.87	69.84	55.97

core components of our approach: Amplitude Spectrum Fusion module (ASF), Phase Spectrum Correction module (PSC), and Multi-Stage Fusion (MSF).

a) Main Modules: Eight model variants (see Table IV) were tested. The baseline variant (I), which replaces MSF with early fusion and substitutes the PAD (ASF+PSC) with pixel-wise additive fusion, achieves the lowest mIoU (54.98%). Enabling MSF alone (II) improves mIoU by 0.39%, while using ASF alone (III) attains 55.86% mIoU, and solely PSC (IV) adds a smaller gain. Combining MSF with either ASF (V) or PSC (VI) yields similar improvements (mIoU around 56.11–56.12%). Integrating all components achieves the best performance (56.26% mIoU), demonstrating the effective synergy of all modules.

b) Loss Function Weights: We conducted weight ablation studies (see Table V) to examine the impact of the trade-off between the amplitude consistency loss (\mathcal{L}_{amp}) and the segmentation loss (\mathcal{L}_{seg}). The best performance (mIoU = 56.26%) is achieved with $\lambda_1 = 0.4$ and $\lambda_2 = 0.1$. Increasing λ_1 above 0.4 degrades performance, notably in under-represented classes, while an overly low λ_2 significantly diminishes performance, confirming that segmentation supervision must remain the dominant objective.

c) Initial Frequency Radius: The initial frequency radius parameter r , which controls the proportion of preserved low-frequency components in our phase-aware filtering, was varied (see Table VI). Our experiments show that $r = 0.1$ achieves an optimal balance (56.26% mIoU). Values that overly suppress low-frequency information or over-smooth the features lead to

TABLE VI
ABLATION RESULTS (%) ON THE INITIAL FREQUENCY RADIUS ON WHU-OPT-SAR.

Configuration	IoU per Category							aAcc	Kappa	mF1	mIoU
	Farmland	City	Village	Water	Forest	Road	Others				
$radius = 0.01$	70.08	57.44	49.31	66.29	84.18	43.08	22.25	84.66	53.92	69.88	56.09
$radius = 0.1$	69.85	58.09	49.71	65.39	84.05	43.24	23.47	84.56	53.96	70.14	56.26
$radius = 1$	69.79	58.19	49.71	64.81	84.15	43.44	23.03	84.52	53.88	70.04	56.16
$radius = 10$	69.71	57.71	49.69	<u>65.63</u>	84.18	43.21	23.56	<u>84.57</u>	<u>53.93</u>	<u>70.12</u>	<u>56.24</u>
$radius = 100$	<u>69.90</u>	57.23	49.57	65.23	84.13	<u>43.34</u>	22.94	<u>84.53</u>	53.88	<u>69.93</u>	<u>56.05</u>

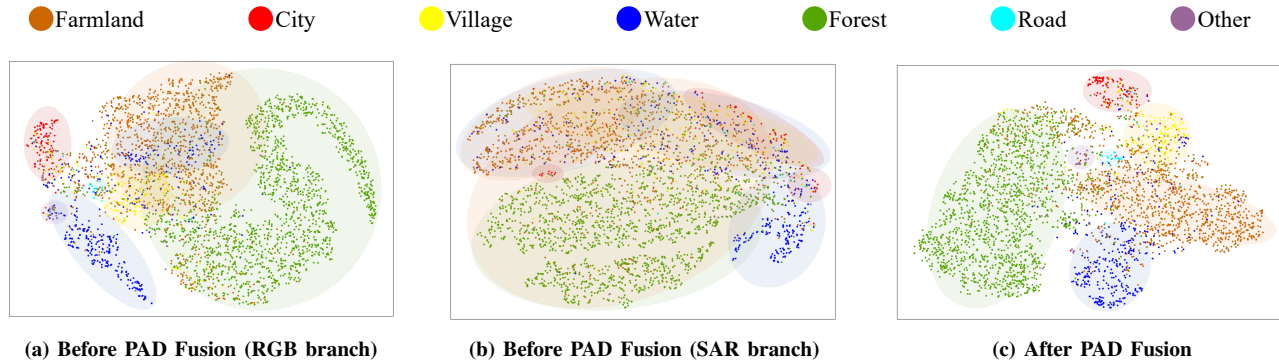


Fig. 8. **t-SNE Visualization of Cross-modal Feature Distribution Evolution.** (a) RGB encoder features exhibit spectral continuity but have blurred boundaries; (b) SAR encoder features, while strongly sensitive to geometry, are affected by speckle noise; (c) PAD-fused features display enhanced intra-class compactness and improved semantic separation.

inferior performance, though the method remains robust for $r \in [0.1, 10]$.

D. Visualization at Distribution Level

To further analyze the feature distribution, we extracted multi-scale features from the RGB and SAR encoders, as well as from the fusion modules. After upsampling to the original resolution, the features were concatenated channel-wise. To balance computational efficiency with preserving discriminative information, a two-stage dimensionality reduction was applied: 1) random spatial sampling, followed by 2) principal component analysis (PCA), retaining 50 principal components (accounting for over 89% of the variance). The final visualization was generated using t-SNE [54] (with a perplexity of 30 and 1,000 iterations).

As illustrated in Fig. 8, the PAD-fused features exhibit enhanced intra-class compactness and improved inter-class separability. Quantitatively, the mean intra-class standard variance is reduced by 20.39% for Road, 13.16% for Water, 6.46% for Forest, and 4.43% for Farmland, compared to the best unimodal baselines. In addition, significant increases in Euclidean distances between critical class pairs, such as a 75.75% increase in the City/Village pair (66.56 to 116.95) and a 13.29% increase for the Farmland/Forest pair (107.64 to 121.89), indicate that the fused features capture cross-modal discriminative patterns effectively.

Overall, these experimental results confirm that the PAD framework significantly improves classification accuracy and prediction consistency by effectively integrating multi-modal information and suppressing noise, while maintaining the

discriminative spectral and geometric characteristics inherent in the data.

V. CONCLUSION

In this paper, we proposed the Phase-Amplitude Decoupling (PAD) framework for fusing SAR and RGB modalities in land cover classification. Our frequency-domain analysis revealed that phase components are consistent across modalities, while amplitude spectra capture modality-specific details, providing the first quantitative physical prior for multi-source remote sensing fusion. PAD separates and aligns phase features while adaptively fusing amplitude components. The Phase Spectrum Correction (PSC) module resolves structural discrepancies, and the Amplitude Spectrum Fusion (ASF) module dynamically integrates SAR's high-frequency details with RGB's low-frequency context. Extensive experiments demonstrate that PAD outperforms existing methods in both accuracy and robustness. Future work will focus on improving phase alignment, particularly under significant geometric distortions due to imprecise cross-modal registration.

REFERENCES

- [1] G. Liu, B. Liu, G. Zheng, and X. Li, "Environment monitoring of shanghai nanhui intertidal zone with dual-polarimetric SAR data based on deep learning," *IEEE Trans. Geosci. Remote. Sens.*, vol. 60, pp. 1–18, 2022.
- [2] L. Gao, Y. Guo, and X. Li, "Weekly green tide mapping in the yellow sea with deep learning: integrating optical and synthetic aperture radar ocean imagery," *Earth Syst. Sci. Data.*, vol. 16, no. 9, pp. 4189–4207, 2024.
- [3] J. Li, D. Hong, L. Gao, J. Yao, K. Zheng, B. Zhang, and J. Chanussot, "Deep learning in multimodal remote sensing data fusion: A comprehensive review," *Int. J. Appl. Earth Obs. Geoinformation*, vol. 112, p. 102926, 2022.

- [4] Y. Ye, J. Zhang, L. Zhou, J. Li, X. Ren, and J. Fan, "Optical and SAR image fusion based on complementary feature decomposition and visual saliency features," *IEEE Trans. Geosci. Remote. Sens.*, vol. 62, pp. 1–15, 2024.
- [5] X. Ma, X. Zhang, M. Pun, and M. Liu, "A multilevel multimodal fusion transformer for remote sensing semantic segmentation," *IEEE Trans. Geosci. Remote. Sens.*, vol. 62, pp. 1–15, 2024.
- [6] S. Xiao, P. Wang, W. Diao, X. Rong, X. Li, K. Fu, and X. Sun, "Mocg: Modality characteristics-guided semantic segmentation in multimodal remote sensing images," *IEEE Trans. Geosci. Remote. Sens.*, vol. 61, pp. 1–18, 2023.
- [7] X. Zhong, T. Lu, W. Huang, M. Ye, X. Jia, and C. Lin, "Grayscale enhancement colorization network for visible-infrared person re-identification," *IEEE Trans. Circuits Syst. Video Technol.*, vol. 32, no. 3, pp. 1418–1430, 2022.
- [8] D. Hong, L. Gao, N. Yokoya, J. Yao, J. Chanussot, Q. Du, and B. Zhang, "More diverse means better: Multimodal deep learning meets remote-sensing imagery classification," *IEEE Trans. Geosci. Remote. Sens.*, vol. 59, no. 5, pp. 4340–4354, 2021.
- [9] T. Chen, S. Kornblith, M. Norouzi, and G. E. Hinton, "A simple framework for contrastive learning of visual representations," in *Proc. Int. Conf. Mach. Learn.*, 2020, pp. 1597–1607.
- [10] Z. Zhao, H. Bai, J. Zhang, Y. Zhang, S. Xu, Z. Lin, R. Timofte, and L. Van Gool, "Cdfuse: Correlation-driven dual-branch feature decomposition for multi-modality image fusion," in *Proc. IEEE/CVF Conf. Comput. Vis. Pattern Recognit.*, 2023, pp. 5906–5916.
- [11] C. Wang, N. Yang, and X. Li, "Advancing forecasting capabilities: A contrastive learning model for forecasting tropical cyclone rapid intensification," *Proc. Nat. Acad. Sci.*, vol. 122, no. 4, p. e2415501122, 2025.
- [12] X. Li, G. Zhang, H. Cui, S. Hou, Y. Chen, Z. Li, H. Li, and H. Wang, "Progressive fusion learning: A multimodal joint segmentation framework for building extraction from optical and sar images," *ISPRS J. Photogramm. Remote Sens.*, vol. 195, pp. 178–191, 2023.
- [13] J. Fu, J. Liu, H. Tian, Y. Li, Y. Bao, Z. Fang, and H. Lu, "Dual attention network for scene segmentation," in *Proc. IEEE/CVF Conf. Comput. Vis. Pattern Recognit.*, 2019, pp. 3146–3154.
- [14] Y. Yuan, X. Chen, and J. Wang, "Object-contextual representations for semantic segmentation," in *Proc. Eur. Conf. Comput. Vis.*, 2020, pp. 173–190.
- [15] T. Wu, S. Tang, R. Zhang, J. Cao, and Y. Zhang, "CGNet: A light-weight context guided network for semantic segmentation," *IEEE Trans. Image Process.*, vol. 30, pp. 1169–1179, 2021.
- [16] E. Xie, W. Wang, Z. Yu, A. Anandkumar, J. M. Álvarez, and P. Luo, "Segformer: Simple and efficient design for semantic segmentation with transformers," in *Adv. Neural Inf. Process. Syst.*, 2021, pp. 12 077–12 090.
- [17] S. Zheng, J. Lu, H. Zhao, X. Zhu, Z. Luo, Y. Wang, Y. Fu, J. Feng, T. Xiang, P. H. S. Torr, and L. Zhang, "Rethinking semantic segmentation from a sequence-to-sequence perspective with transformers," in *Proc. IEEE/CVF Conf. Comput. Vis. Pattern Recognit.*, 2021, pp. 6881–6890.
- [18] B. Cheng, I. Misra, A. G. Schwing, A. Kirillov, and R. Girdhar, "Masked-attention mask transformer for universal image segmentation," in *Proc. IEEE/CVF Conf. Comput. Vis. Pattern Recognit.*, 2022, pp. 1280–1289.
- [19] J. Xu, Z. Xiong, and S. P. Bhattacharyya, "PIDNet: A real-time semantic segmentation network inspired by PID controllers," in *Proc. IEEE/CVF Conf. Comput. Vis. Pattern Recognit.*, 2023, pp. 19 529–19 539.
- [20] J. Chen, J. Mei, X. Li, Y. Lu, Q. Yu, Q. Wei, X. Luo, Y. Xie, E. Adeli, Y. Wang, M. P. Lungren, S. Zhang, L. Xing, L. Lu, A. L. Yuille, and Y. Zhou, "TransUNet: Rethinking the U-Net architecture design for medical image segmentation through the lens of transformers," *Medical Image Anal.*, vol. 97, p. 103280, 2024.
- [21] W. Li, K. Sun, W. Li, X. Huang, J. Wei, Y. Chen, W. Cui, X. Chen, and X. Lv, "Assisted learning for land use classification: The important role of semantic correlation between heterogeneous images," *ISPRS J. Photogramm. Remote Sens.*, vol. 208, pp. 158–175, 2024.
- [22] L. H. Hughes, M. Schmitt, L. Mou, Y. Wang, and X. X. Zhu, "Identifying corresponding patches in SAR and optical images with a pseudo-siamese CNN," *IEEE Geosci. Remote. Sens. Lett.*, vol. 15, no. 5, pp. 784–788, 2018.
- [23] X. Li, G. Zhang, H. Cui, S. Hou, S. Wang, X. Li, Y. Chen, Z. Li, and L. Zhang, "MCANet: A joint semantic segmentation framework of optical and SAR images for land use classification," *Int. J. Appl. Earth Obs. Geoinformation*, vol. 106, p. 102638, 2022.
- [24] B. Ren, S. Ma, B. Hou, D. Hong, J. Chanussot, J. Wang, and L. Jiao, "A dual-stream high resolution network: Deep fusion of GF-2 and GF-3 data for land cover classification," *Int. J. Appl. Earth Obs. Geoinformation*, vol. 112, p. 102896, 2022.
- [25] H. Zhang, X. Zuo, J. Jiang, C. Guo, and J. Ma, "MRFS: Mutually reinforcing image fusion and segmentation," in *Proc. IEEE/CVF Conf. Comput. Vis. Pattern Recognit.*, 2024, pp. 26 964–26 973.
- [26] J. Zhang, H. Liu, K. Yang, X. Hu, R. Liu, and R. Stiefelhagen, "CMX: cross-modal fusion for RGB-X semantic segmentation with transformers," *IEEE Trans. Intell. Transp. Syst.*, vol. 24, no. 12, pp. 14 679–14 694, 2023.
- [27] P. Zhang, B. Peng, C. Lu, Q. Huang, and D. Liu, "ASANet: Asymmetric semantic aligning network for rgb and sar image land cover classification," *ISPRS J. Photogramm. Remote Sens.*, vol. 218, pp. 574–587, 2024.
- [28] Y. Wang, W. Huang, F. Sun, T. Xu, Y. Rong, and J. Huang, "Deep multimodal fusion by channel exchanging," in *Adv. Neural Inf. Process. Syst.*, 2020.
- [29] X. Zhong, Z. Li, S. Chen, K. Jiang, C. Chen, and M. Ye, "Refined semantic enhancement towards frequency diffusion for video captioning," in *Proc. AAAI Conf. Artif. Intell.*, 2023, pp. 3724–3732.
- [30] Y. Zhou, Y. Feng, S. Huo, and X. Li, "Joint frequency-spatial domain network for remote sensing optical image change detection," *IEEE Trans. Geosci. Remote. Sens.*, vol. 60, pp. 1–14, 2022.
- [31] C. Tian, Q. Zhang, G. Sun, Z. Song, and S. Li, "FFT consolidated sparse and collaborative representation for image classification," *Arab. J. Sci. Eng.*, vol. 43, pp. 741–758, 2018.
- [32] A. V. Oppenheim and J. S. Lim, "The importance of phase in signals," *Proceedings of the IEEE*, vol. 69, no. 5, pp. 529–541, 1981.
- [33] Z. Zhao, B. Zuo, and Y. Wang, "Music conditioned generation for human-centric video," *IEEE Signal Process. Lett.*, vol. 31, pp. 506–510, 2024.
- [34] X. Huang and S. J. Belongie, "Arbitrary style transfer in real-time with adaptive instance normalization," in *Proc. IEEE/CVF Int. Conf. Comput. Vis.*, 2017, pp. 1510–1519.
- [35] X. Jin, C. Lan, W. Zeng, Z. Chen, and L. Zhang, "Style normalization and restitution for generalizable person re-identification," in *Proc. IEEE/CVF Conf. Comput. Vis. Pattern Recognit.*, 2020, pp. 3140–3149.
- [36] G. Chen, P. Peng, L. Ma, J. Li, L. Du, and Y. Tian, "Amplitude-phase reconstruction: Rethinking robustness of convolutional neural networks in frequency domain," in *Proc. IEEE/CVF Int. Conf. Comput. Vis.*, 2021, pp. 448–457.
- [37] S. Lee, J. Bae, and H. Y. Kim, "Decompose, adjust, compose: Effective normalization by playing with frequency for domain generalization," in *Proc. IEEE/CVF Conf. Comput. Vis. Pattern Recognit.*, 2023, pp. 11 776–11 785.
- [38] L. Chi, B. Jiang, and Y. Mu, "Fast fourier convolution," in *Adv. Neural Inf. Process. Syst.*, 2020.
- [39] L. Kong, J. Dong, J. Ge, M. Li, and J. Pan, "Efficient frequency domain-based transformers for high-quality image deblurring," in *Proc. IEEE/CVF Conf. Comput. Vis. Pattern Recognit.*, 2023, pp. 5886–5895.
- [40] Y. Rao, W. Zhao, Z. Zhu, J. Lu, and J. Zhou, "Global filter networks for image classification," in *Adv. Neural Inf. Process. Syst.*, 2021, pp. 980–993.
- [41] J. Guibas, M. Mardani, Z. Li, A. Tao, A. Anandkumar, and B. Catanzaro, "Adaptive fourier neural operators: Efficient token mixers for transformers," *arXiv preprint arXiv:2111.13587*, 2021.
- [42] Y. Xiao, Q. Yuan, K. Jiang, Y. Chen, Q. Zhang, and C. Lin, "Frequency-assisted mamba for remote sensing image super-resolution," *IEEE Trans. Multimedia*, 2024.
- [43] H. Cheng, S. Yang, J. T. Zhou, L. Guo, and B. Wen, "Frequency guidance matters in few-shot learning," in *Proc. IEEE/CVF Int. Conf. Comput. Vis.*, 2023, pp. 11 780–11 790.
- [44] F. Yu, Y. Zhang, H. Li, C. Du, L. Liu, and M. Jiang, "Phase contour enhancement network for clothing parsing," *IEEE Trans. Consumer Electron.*, vol. 70, no. 1, pp. 2784–2793, 2024.
- [45] S. Lin, Z. Zhang, Z. Huang, Y. Lu, C. Lan, P. Chu, Q. You, J. Wang, Z. Liu, A. Parulkar, V. Navkal, and Z. Chen, "Deep frequency filtering for domain generalization," in *Proc. IEEE/CVF Conf. Comput. Vis. Pattern Recognit.*, 2023, pp. 11 797–11 807.
- [46] L. Chen, Y. Fu, L. Gu, C. Yan, T. Harada, and G. Huang, "Frequency-aware feature fusion for dense image prediction," *IEEE Trans. Pattern Anal. Mach. Intell.*, vol. 46, no. 12, pp. 10 763–10 780, 2024.
- [47] Y. Wang, H. Wang, L. Wang, X. Wang, L. Zhu, W. Lu, and H. Huang, "Complementary advantages: Exploiting cross-field frequency correlation for nir-assisted image denoising," *arXiv preprint arXiv:2412.16645*, 2024.
- [48] N. Wright, J. M. Duncan, J. N. Callow, S. E. Thompson, and R. J. George, "Training sensor-agnostic deep learning models for remote sensing: Achieving state-of-the-art cloud and cloud shadow identification with omnisclocloudmask," *Remote Sens. Environ.*, vol. 322, p. 114694, 2025.

- [49] J. W. Cooley and J. W. Tukey, "An algorithm for the machine calculation of complex fourier series," *Math. Comp.*, vol. 19, no. 90, pp. 297–301, 1965.
- [50] A. L. Maas, A. Y. Hannun, and A. Y. Ng, "Rectifier nonlinearities improve neural network acoustic models," in *Proc. Int. Conf. Mach. Learn.*, 2013, p. 3.
- [51] M. Contributors, "MMSegmentation: Openmmlab semantic segmentation toolbox and benchmark. 2020," 2023.
- [52] I. Loshchilov and F. Hutter, "Decoupled weight decay regularization," in *Proc. Int. Conf. Learn. Represent.*, 2019.
- [53] Y. Wang, X. Chen, L. Cao, W. Huang, F. Sun, and Y. Wang, "Multimodal token fusion for vision transformers," in *Proc. IEEE/CVF Conf. Comput. Vis. Pattern Recognit.*, 2022, pp. 12 176–12 185.
- [54] L. Van der Maaten and G. Hinton, "Visualizing data using t-sne," *J. Mach. Learn. Res.*, vol. 9, no. 11, 2008.